ChemMedChem

Research Article
doi.org/10.1002/cmdc.202200244

Chemistry Europe
European Chemical Societies Publishing

www.chemmedchem.org

Tunable Emissive Ir(III) Benzimidazole-quinoline Hybrids as Promising Theranostic Lead Compounds

Marta Redrado,[a] Miriam Miñana,[a] Michael P. Coogan,*[b] M. Concepción Gimeno,*[a] and Vanesa Fernández-Moreira*[a]

Bioactive and luminescent cyclometallated Ir(III) complexes $[Ir(ppy)_2\mathbf{L1}]Cl$ (**1**) and $[Ir(ppy)_2\mathbf{L2}]Cl$ (**2**) containing a benzimidazole derivative (**L1**/**L2**) as auxiliary mimic of a nucleotide have been synthesised. The emissive properties of both complexes are conditioned by the nature of **L1** and **L2**, rendering an orange and a green emitter respectively. Both are highly emissive with quantum yield increasing in absence of oxygen up to 0.26 (**1**) and 0.36 (**2**), suggesting their phosphorescent character. Antiproliferative activity against lung cancer A549 cells increased up to 15 times upon irradiation conditions, reaching IC_{50} values in the nanomolar range (0.3 ± 0.09 μM (**1**) and 0.26 ± 0.14 μM (**2**)) and pointing them as good PSs candidates for photodynamic therapy via $^1O_2$ generation. Cellular biodistribution analysis by fluorescence microscopy suggest the lysosomes as the preferential accumulation organelle. Time-resolved studies showed a greatly increased cellular emission lifetime compared to the solution values, indicating binding to macromolecules or cellular structures and restriction of collision and vibrational quenching.

Introduction

The necessity of finding additional metallodrugs to cisplatin is boosting research into new, and very promising, metal-based structures such as those derived from Ru(II), Au(I/III), very recently Ir(III)[1] or combination of those.[2–4] The key point is to deliver drugs able to reveal their therapeutic potential by a mechanism of action different from that of cisplatin, in order to avoid the so-called 'platinum resistance'[5] and its adverse side effects.[6] Cyclometallated Ir(III) complexes with the general formula $[Ir(C^\wedge N)_2(N^\wedge N)]^+$, present a variety of cellular targets, from mitochondria[7] or lysosomes to endoplasmic reticulum among others organelles,[8] thus triggering different cellular therapeutic response.[9] The nature of the cyclometallated ($C^\wedge N$) and ancillary ligands ($N^\wedge N$) together with the possibilities of their further functionalisation, seems to be crucial for directing the complexes towards a specific target and, in consequence, for modulating the mechanism of action. Initially, cyclometallated Ir(III) complexes were proposed as alternative cellular markers to organic fluorophores,[10] due to their rich photophysical properties. However, the specific biological behaviour shown by many of them in terms of biological sensing and therapy, has opened the scope of the investigations to these new areas.[11]

Regarding cellular visualisation, fluorescence microscopy and, more recently, Fluorescence Lifetime Imaging (or Mapping) known as FLIM are techniques widely used to monitor localisation or response to stimuli at the sub-cellular level,[12] relaying on the emission and excited state lifetimes of the markers respectively. In this sense, *d*-block metal phosphorescent probes, and in particular, iridium based complexes possess excellent photophysical properties for both techniques.[13] Their large Stokes' shifts, emission tuneability, lifetimes within the microsecond domain and high thermal and kinetic stability as well as their low photobleaching are some of the most representative features.

Alternatively, regarding the use of iridium complexes in therapy, they have revealed their great prospects as one- and two- photon photosensitisers (PSs) in photodynamic therapy.[14,15] Their rich photophysical properties embrace some of crucial requirements for PSs, such as high spin-orbit coupling constant that favours intersystem crossing and renders long PS triplet excited state lifetimes, as well as an appropriate energy gap for excitation of $^3O_2$ to deliver the highly toxic $^1O_2$ molecules.[16]

In the context of theranosis, the fact that iridium complexes, such as those in the present study, may offer both photocontrolled cytotoxicity and photoluminescence renders exciting opportunities for complementarity between studying the cellular behaviours of the complexes, via fluorescence imaging, and developing their therapeutic potential via the understanding gained. In particular, the triplet nature of emission from these complexes leads to long luminescence lifetimes, which can offer additional advantages in imaging studies which are

[a] M. Redrado, M. Miñana, Prof. M. Concepción Gimeno, Dr. V. Fernández-Moreira
Departamento de Química Inorgánica
Instituto de Síntesis Química y Catálisis Homogénea (ISQCH)
CSIC-Universidad de Zaragoza
Pedro Cerbuna 12, 50009 Zaragoza (Spain)
E-mail: gimeno@unizar.es
vanesa@unizar.es

[b] Dr. M. P. Coogan
Department of Chemistry
Lancaster University, LA1 4YB Lancaster (UK)
E-mail: m.coogan@lancaster.ac.uk

Supporting information for this article is available on the WWW under https://doi.org/10.1002/cmdc.202200244

not available with short-lived singlet emitters.[13] Amongst the advantages offered by long-lived luminophores are the ability to differentiate emission from the imaging agent from auto-fluorescence *via* time-gated experiments,[17] in which only long-lived emission is involved, removing all short lifetime signals. More interestingly, longer lifetimes offer the possibility of using the cellular emission lifetime to obtain information about the cellular environment, which is best known in the long established application of measuring cellular oxygen concentration, $[O_2]$,[18] via quenching of emission from phosphorescent emission to give shortened lifetimes.[19] Fluorescence lifetime imaging, FLIM,[20,21] is a common technique in bioimaging in which a colour scale for an image is mapped not by the wavelength or intensity of light at a certain pixel, but by the lifetime of the emission detected at that position after excitation by a pulse of light. Typically, the lifetime of fluorescence is calculated from the rate of decay of the emission measured using Time-Resolved Single Photon Counting (TRSPC) techniques, which are applicable to very fast decays (i.e. short lifetimes associated with singlet excited states).[22] The more recently developed equivalent for longer-lived, triplet systems, Phosphorescent Lifetime Imaging Microscopy, PLIM, is based on the same approaches of mapping by lifetime, and there have been some interesting biological applications.[23]

As previously mentioned, the structural design step for developing Ir(III) complexes that can be used in therapy and visualisation is key. In this sense, benzimidazole is an important structural motif found in many natural and pharmacological active molecules[24] due to the structural and electronic similarity to nucleotides.[25] For that reason, they can be considered as mimics of a nucleotide making them prone to be easily recognised and accepted by the body, while delivering a new set of different properties to that expected for a nucleotide. There is a wide range of Ir(III) complexes that have relied on the good prospects of benzimidazole derivatives for therapeutic applications.[26–28] Benzimidazole derivatives have been used as either cyclometallated (C^N) and/or ancillary diimine (N^N) ligand rendering diverse optical and bioactive properties to the Ir(III) complexes, see Figure 1. In addition, the imidazole ring can be funtionalised through the reactive N–H group to incorporate additional features that could affect directly to the photophysics[29,30] or biological interaction.[31] Specifically, this work intends to provide new insights of the therapeutic potential against lung cancer A549 cells of novel cyclometallatated iridium complexes containing a derivatised benzimidazole with a planar organic chromophore. Moreover, thorough cellular biodistribution studies by fluorescence microscopy and FLIM/PLIM techniques will assess the great feasibility of iridium complexes for being used within diverse visualisation techniques and ultimately in theranosis.

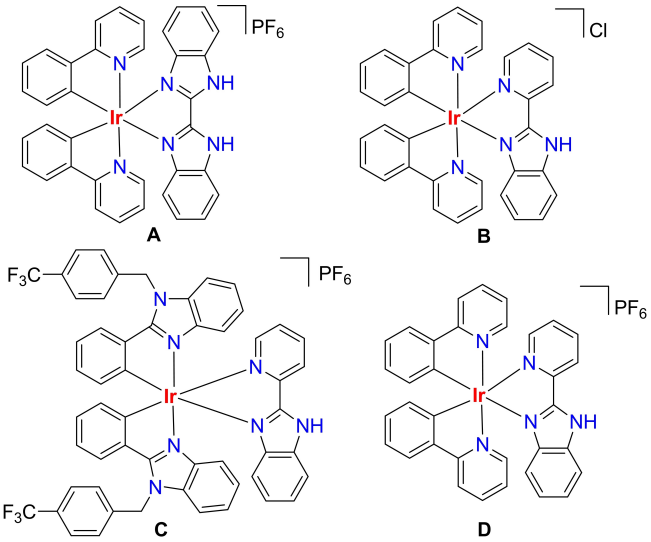

Figure 1. Examples of benzimidadole iridium-based complexes A,[26] B,[32] C[27] and D.[33]

Results and Discussion

Synthesis and general characterization

The synthetic approach for developing Ir(III) complexes that can act as photosensitizers (PS) and cell imaging probes by fluorescence microscopy and FLIM/PLIM entails the use of 2-(2-pyridyl)benzimidazole (PyBzIm) or 2-(4-thiazolyl)benzimidazole (TzBzIm) as a linker between the cyclometallated Ir(III) core and the blue-purple organic chromophore, 2-methylquinoline. Thus, both benzimidazole derivatives coordinate the iridium metal centre in a N^N chelate fashion, whereas the binding of the organic chromophore would be through the benzimidazolyl N–H group.

The synthesis begins with the preparation of ligands **L1** and **L2**, see Scheme 1. Both of them were prepared following a slightly modified procedure previously described by Shavaleev[34] and Vaquero[35] for similar compounds. Specifically, benzimidazole derivatives were mixed with an excess of base, (K_2CO_3 in DMF in the case of **L1** and KOH in CH_3CN for **L2**) to assist the nucleophilic substitution reaction that takes places thereafter the addition of 2-chloromethylquinoline. Then, **L1** and **L2** were refluxed with $[Ir(ppy)_2(\mu\text{-}Cl)]_2$ obtaining complexes **1** and **2** respectively, in moderated yields as detailed in experimental section. Their expected structures were corroborated using ^1H and $^{13}C\{^1H\}$ NMR spectroscopy (Figure 2 and S1–S15) and assignation of the peaks was also possible by means of two-dimensional (2D) NMR experiments (^1H-COSY, HSQC and HMBC). Both complexes have C_1 molecular symmetry as well as a helicoidal chirality implicit in the trichelated octahedral complexes. Their asymmetric nature due to presence of a **L1** and **L2**, leaded to the non-equivalence of the two phenyl-pyridines (ppy) in each complex, rendering two set of different signals in ^1H and ^{13}C-NMR for the ppy. Consequently, the singlet observed for the protons of CH_2 group in the ligands **L1** and **L2**

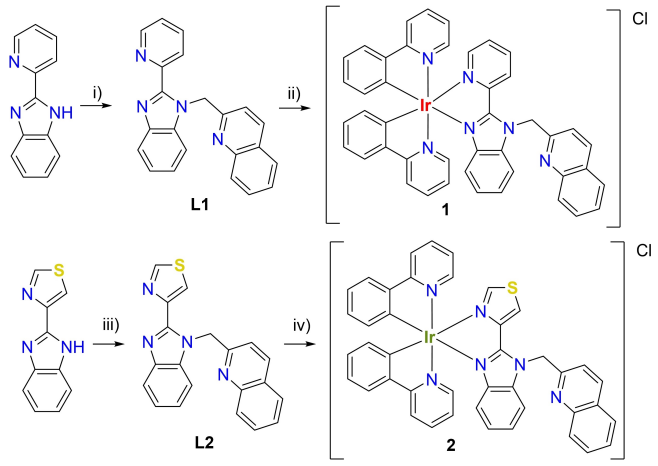

Scheme 1. Synthetic pathway for the synthesis of **L1** and **L2**, and complexes **1** and **2**. Reaction conditions as follow: i) 2-chloromethylquinoline, K_2CO_3, DMF, r.t., 48 h; ii) $[Ir(ppy)_2(\mu\text{-}Cl)]_2$, DCM:MeOH (1 : 3), reflux, 24 h; iii) 2-chloromethylquinoline, KOH, CH_3CN, r.t., 48 h; iv) $[Ir(ppy)_2(\mu\text{-}Cl)]_2$, DCM, reflux, 24 h.

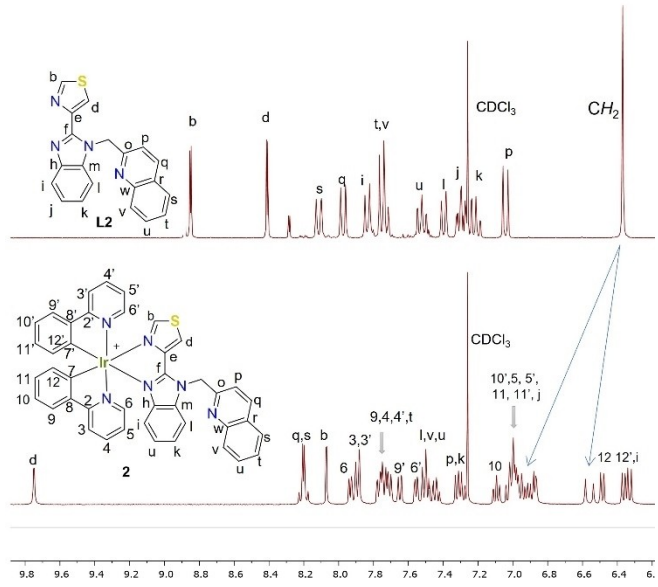

Figure 2. ^{1}H-NMR (400 MHz) spectra of **L2** and complex **2** recorded in $CDCl_3$.

at c.a. 6.4 ppm is transformed into two diastereotopic protons mutually coupled doublets at lower field upon coordination to the Ir(III) (6.6 ppm and around 7.0 ppm obscured by other protons), see Figure 2 for comparison between ^{1}H-NMR spectra of **L2** and **2**. Regarding the ppy ligand, a clear shielding of protons H6, H6′ was observed after coordination of the **L1** and **L2** from over 9 ppm in $[Ir(ppy)_2(\mu\text{-}Cl)]_2$[36] to below 8 ppm in both cases. Similarly, Hj of **L1** and Hi **L2** suffer a clear shielding upon coordination with the Ir(III) core, from c.a 7.90 and 7.84 ppm to 6.35 and 6.31 ppm in complex **1** and **2** respectively. Additional analytical data provided by mass spectrometry corroborated the accomplishment of the synthesis of both complexes, see experimental section and Figures S16, S17.

Optical properties

Photophysical properties of complexes **1** and **2** were measured in aerated and degassed DMSO solution at room temperature (r.t.). UV-vis absorption bands (λ_{em}) and their extinction coefficients (ε) emission and excitation maxima wavelengths (λ_{em}, λ_{exc}), excited state lifetimes (ζ) quantum yields (Φ) and radiative (κ_r) and non-radiative (κ_{nr}) rate constants are collected in Table 1. The UV-vis absorption spectra of both complexes exhibit intense broad absorption bands around 265 nm that are attributed to spin allowed (π→π*) ligand centred transitions (^{1}LC) within the N^N and C^N ligands as well as within the quinoline fragment. In addition, the less intense absorption bands appearing between 315 and 385 nm are assigned to both, (n→π*) transitions in the benzimidazole and quinoline fragments, as well as charge transfer transitions, and specifically, to ligand to ligand charge transfer transition (^{1}LLCT), a transition from the orthometallated C^N (π)→N^N(*π) ligand, as well as metal to ligand charge transfer transition (^{1}MLCT) from the Ir(dπ)→N^N(π*). Finally, the less energetic bands appearing over 400 nm are generally associated with spin forbidden ^{3}MLCT, ^{3}LLCT and ^{3}LC transitions as consequence of the strong spin-orbit coupling provided by the iridium atom[37] Regarding the emission properties, both complexes revealed a distinct emission profile, see Figure 3. Whereas complex **1** displayed a broad emission band centred at 604 nm rendering, therefore, an orange colour, complex **2** showed a structured emission with maxima at 486 and 513 nm, being in this case a green emitter. Such distinct pattern may suggest a different emission origin for both complexes. Generally, the non-structured profile indicates an emission with a charge transfer (CT) character meanwhile the structured pattern is associated with emissive states with large ^{3}LC character.[38] Therefore, it can be suggested that, in this specific case, the substitution of a 2-(2-pyridyl)-benzimidazole derivative in complex **1** for a 2-(4-thiazolyl)benzimidazole derivative in complex **2** is changing the origin of the emission from a mixture of ^{3}LLCT and ^{3}MLCT in the first case to a more ^{3}LC character in the second one. Probably the enhanced electron donating nature of the thiazole ring in comparison to that of the pyridine due to the presence of a sulfur atom, that contributes with an additional electron lone pair to the aromatic π system, leads to the destabilisation of the LUMO orbitals which is generally centred in the N^N ancillary

Table 1. Photophysical properties for complexes **1** and **2** in DMSO solution at 298 K.

	λ UV-vis[a] nm (ε×10^3/ dm^3 mol^{-1} cm^{-1})	λ_{em} (λ_{exc})[a] (nm)	ζ[a] (ns)	Φ[a] (%)	κ_r (×10^5) (s^{-1})	κ_{nr} (×10^5) (s^{-1})	Φ[b] (%)
1	264 (23.2), 318 (18.3), 378 (3.4), 373 (4.3)	604 (422)	376	12.50	3.29	23.3	26
2	267 (20.9), 305 (17.6), 384 (3.3)	486, 513 (336)	436	8.50	0.085	269.8	38

[a] Aerated DMSO solution, 1.5×10^{-5} M. [b] Deoxygenated DMSO solution. $K_r = \Phi/\zeta$ and $K_{nr} = (1-\Phi)/\zeta$[40]

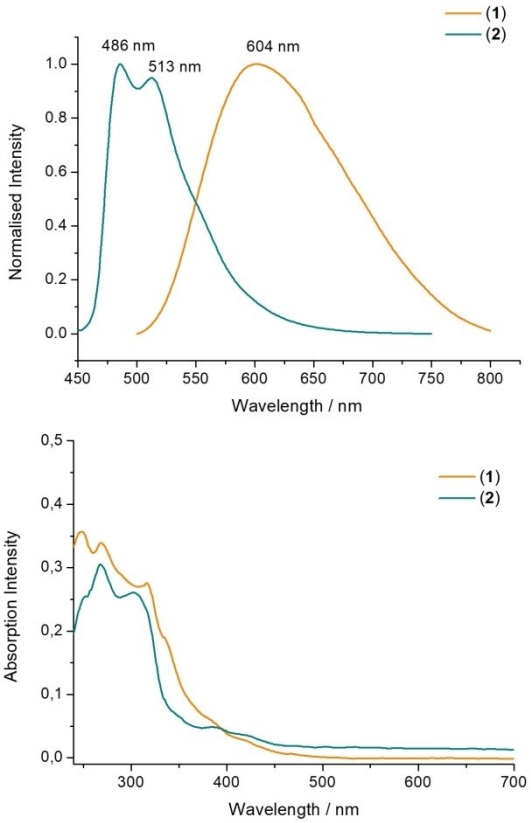

Figure 3. Emission and UV-absorption spectra of complexes **1** and **2** recorded in DMSO (1.5×10^{-5} M) at 298 K.

ligand.[39] Such destabilisation causes the different emissive state origin going from a ^{3}MLCT/^{3}LLCT in **1** to ^{3}LC in **2**, as Espino, Bolink and Ortí demonstrated with a thorough theoretical study of similar Ir(III) complexes.[39] Moreover, this data reveals that the presence of the quinoline fragment is not affecting the overall emission of the complexes.

Excited state lifetimes in aerated DMSO solution were also investigated displaying values of 376 and 436 ns for complexes **1** and **2** respectively suggesting in both cases the expected phosphorescent character. Moreover, the quantum yield of emissions was assessed in presence and absence of oxygen revealing a general increment when oxygen is not present. Specifically, complex **1** emission quantum yield increased from 0.12 to 0.26 whereas complex **2** showed and increment from 0.08 to 0.38 after oxygen removal. Interestingly, calculation of radiative and non-radiative rates[40] indicates that complex **2** has a much faster non-radiative rate than compound **1**. Although many factors can deactivate excited states and contribute to k_{nr}, if this greater rate involves a mechanism concerning deactivation through electron transfer processes that can lead to photochemical reactions, then this may help to explain the greater observed propensity for photobleaching of **2** compared to **1** (see below).

Antiproliferative activity

The *in vitro* antiproliferative character of complexes **1** and **2**, as well as their ligand precursors, **L1** and **L2**, was determined by MTT-reduction assay after 24 h of treatment in lung carcinoma A549 cells. These experiments were performed in parallel in dark and under irradiation conditions (470 nm, 15.2 J·cm^{-2} dose) to assess the suitability of the complexes as possible anticancer agents in either chemotherapy and/or in photodynamic therapy.

Briefly, cells were incubated with the complexes and ligands in the range of 0.2 to 50 μM at 37 °C (5 % CO_2) for approximately 4 h. Afterwards, cell media was changed for a fresh one in both experiments, in order to remove the complex not internalised in the cells at that point. Cells from the dark experiment were placed back at the incubator for further 20 h, whereas cells from the irradiation experiment were treated with monochromatic blue light (470 mn) for 10 min before further 20 h incubation. Cytotoxicity and photocytotoxicities are collected in Table 2 as the half maximal inhibitory concentration (IC_{50}) as well as the phototoxic index (PI), the ratio of the dark to light IC_{50}. Interestingly, **L1** and **L2** did not display cytotoxic activity; however, complexes **1** and **2** presented a high antiproliferative character in dark conditions, yielding IC_{50} values of 4.59 ± 0.23 and 3.50 ± 0.17 μM respectively. These results seem to indicate that the bioactivity falls in the Ir(III) fragment, as it has been previously reported by our research group and others for similar cyclometallated Ir(III) complexes.[28,41] Moreover, the introduction of a thiazolyl instead of a pyridyl within the benzimidazole derivative slightly improves the therapeutic potential of the probes. The low micromolar range of the IC_{50} values found for both complexes in A549 cells in dark conditions are comparable to those reported in the literature for similar cyclometallated Ir(III) complexes,[42] corroborating the good prospects of these benzimidazolyl complexes for chemotherapy purposes in lung cancer.

Interestingly, photocytotoxic analysis for both complexes showed more than 10 times increment of the cytotoxic potential upon irradiating at 470 nm for 10 min, revealing **1** and **2** as potential candidates for photodynamic therapy. In both cases, the complexes reached IC_{50} values of 0.30 ± 0.09 and 0.26 ± 0.14 μM respectively. Similarly to the studies performed in dark conditions, **L1** and **L2** remained unaltered at the studied concentration highlighting, once again, the importance of the metal centre to deliver the cytotoxicity. Making a fair compar-

Table 2. IC_{50} values (μM) of **L1**, **L2**, **1** and **2** incubated in A549 cell during 24 h. Data were obtained from quadruplicates of three independent experiments and expressed as mean values ± standard deviation (SD).

	$IC_{50(Dark)}$	$IC_{50(Irrad.)}$[a]	PI[b]
L1	>50	>50	–
L2	>50	>50	–
1	4.59 ± 0.23	0.30 ± 0.09	15.3
2	3.50 ± 0.17	0.26 ± 0.14	13.5

[a] Irradiation at 470 nm during 10 min, dose of 15.2 J/cm^2. [b] PI: Phototoxic index: ratio between IC_{50} value in dark and IC_{50} value after irradiation, $PI = IC_{50(dark)}/IC_{50\ (irrad.)}$.

ison between the efficiency of the phototherapeutic potential of different complexes challenging, as not only the cell line type and incubation times are decisive, but also the irradiation wavelength and the irradiation time are critical factors to take into account. Despite that, these complexes can be considered promising PSs, in view of their effectiveness using irradiation wavelength over 450 nm that allows deeper penetration,[43] together with the short irradiation times needed[44] and finally the nanomolar IC_{50} range reached.[28,33]

ROS generation

After seeing that the antiproliferative activity increases upon irradiation and knowing that such increment could be due to the presence intracellular reactive oxygen species (ROS), the generation of ROS was assessed by flow cytometry using dihydroethidium (DHE) as internal marker. DHE is a blue fluorescent probe that is oxidized in presence of the superoxide ion to 2-hydroxyethidium (2-HE) rendering a red fluorescence. The assay was performed for complex **2** in dark and under irradiation conditions in order elucidate whether ROS was being generated because of the effect that the irradiation exert on complex **2**. Figure 4 clearly showed the increase of ROS under irradiation conditions. Specifically, the level of the detected 2-HE indicates that irradiation of the cells by their own does not have any effect (graph B in Figure 4). A slight ROS generation increment was observed due to the presence of complex **2** (graph C, Figure 4). But the larger change in the capacity of generating ROS was seen when cells incubated with **2** were irradiated for 10 minutes with a 470 nm light source, graph A, Figure 4, left). The additional two peaks shifted to the right in graph A indicate that two fractions of the cells clearly over-activated their ROS production mechanism. Moreover, the average fluorescent intensity of the dye given for each condition showed an increment of at least three times between both, control cell assays (irradiated (B) and no irradiated conditions (D)) and the irradiated cells incubated with complex **2** (A). Therefore, it can be suggested that the substantial amount of ROS produced upon excitation, might account for the photobiological activity seen.[45] In view of the results, generation of singlet oxygen ($^1O_2$) was specifically addressed to check if such species was being produced because of the complex irradiation. It is known that phosphorescence of $^1O_2$ appears at 1270 nm, therefore, if it produced upon irradiation, an emission band should be visible in the NIR.[46] Direct measurement of emission of $^1O_2$ was then undertaken by steady state fluorescence spectroscopy for complex **2**, see Figure 4. Irradiation of an acetonitrile solution of **2** with a 405 nm picosecond pulsed diode laser, rendered a band centered at 1270 nm, indicative of $^1O_2$ generation. An additional experiment was performed to corroborate that band observed at 1270 nm was not a mere artefact from the spectrometer. Thus, increasing concentrations of complex **2** were irradiated with the same laser diode and monitoring the spectrum from 1200 to 1350 nm demonstrated that growing amount of $^1O_2$ were being produced, see Figure S18.

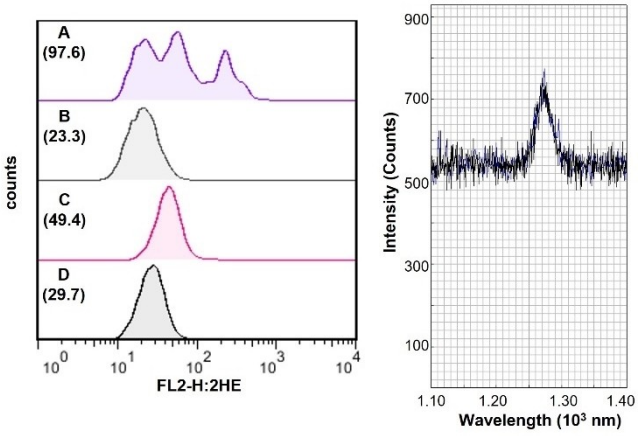

Figure 4. Left: ROS generation assay graphs for different conditions. A) A549 cells initially incubated for 5 hours with complex **2** (0.75 μM), then irradiated for 10 min at 470 nm (dose 15.2 J/cm^2) and further incubation for 19 hours; B) control A549 cells irradiated for 10 min at 470 nm (dose 15.2 J/cm^2); C) A549 cells incubated with the complex **2** (0.75 μM) for 24 h, dark conditions; D) control A549 cells in dark conditions. Value given in brackets, fluorescence intensity average. Right. Detection of $^1O_2$ assay. Emission spectra of a solution of **2** in CH_3CN (1.13 μM) recorded on a PicoQuant, FT300 fluorescence spectrometer after excitation at 405 nm picosecond pulsed diode laser with 80 MHz repetition rate. Detection was performed with a NIR-PMT unit with a spectral range of 950 nm to 1400 nm

Subcellular biodistribution: Fluorescence microscopy

Subcellular biodistribution of complexes **1** and **2** was examined by fluorescence confocal microscopy. Colocalisation experiments using commercial available trackers, LysoTracker Red (LTR) and MitoTracker Deep Red (MTDR), were undertaken in live-cells. The experiment entailed the incubation of the complexes with A549 cells for 2 hours. Then, after addition of the different trackers, cells were visualised upon specific irradiation at 405, 561 and 633 nm to reveal the biodistribution of the complexes, LTR and MTDR respectively. The assays showed that both complexes were able to permeate the cellular membrane and transport to certain distinct areas of the cytoplasm. The biodistribution pattern of the complexes in comparison with that of the MTDR showed that no localisation in the mitochondria occurs, see Figure 5. Instead, when those biodistribution patterns are compared with that of the LTR it is clear that both complexes have a partial localisation in the lysosomes, see superimposition images in Figure 5 and S19. Calculated Pearson coefficient for compound **1** (0.42) and **2** (0.60) corroborates the partial lysosomal localization.[47] Similar lysosomal localisation was also previously seem for Ir(III) complexes containing benzimidazole derivatives as ancillary ligand.[17,28] Moreover, it was observed that both complexes suffer from photobleaching upon irradiation, this being substantially faster in the case of complex **2**. A parallel experiment, where the emission intensity of **1** and **2** in presence of LTR was collected before and after irradiation, corroborated such observation. In both cases the emission intensity drops after

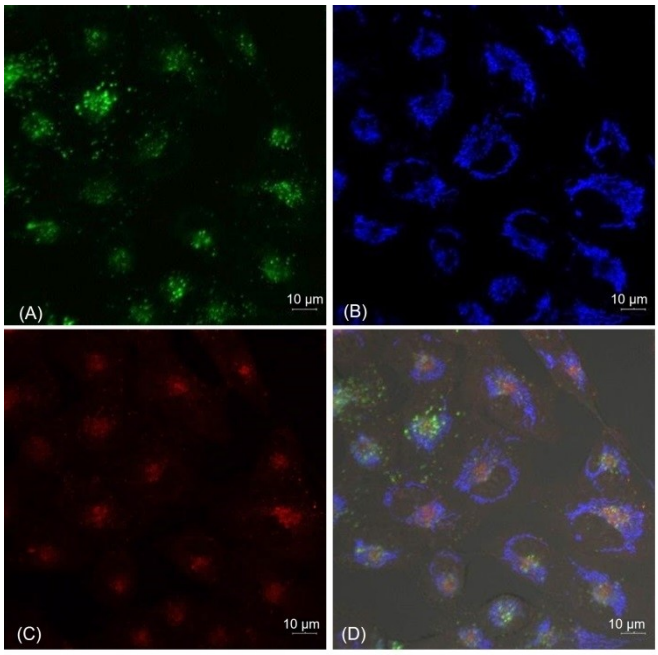

Figure 5. Fluorescence microscopy images of A549 cells incubated with complex **1** (2 μM) for 2 h, MTDR (250 nM) for 45 min and LTR (100 nM) for 45 min. Images recorded after (A) $\lambda_{irra} = 405$ nm (detection window between 482 and 677 nm) to visualise complex **1**; (B) $\lambda_{irra} = 633$ nm (detection window between 638 and 758 nm) to visualise MTDR; (C) $\lambda_{irra} = 561$ nm (detection window between 570 and 615 nm), (D) superimposition image of (A), (B), (C) and bright field.

irradiation, indicating the loss of emissive complex to a photochemical reaction. However, whereas in the case of complex **1** the emission intensity decreased after two cycles of irradiation, in complex **2** the emission reduction is visible almost immediately after the first cycle of irradiation, see Figure S20, indicating greater photochemical reactivity. It is interesting to note that while **2** suffers more from photobleaching than **1**, its phototoxic index is very close to, and slightly lower than, that of **1**. While differences in uptake and localisation will influence the PI, this anomaly may suggest that the photochemical reaction leading to photobleaching could be different to the one responsible for phototoxicity.

Cellular biodistribution: FLIM

In addition to standard confocal microscopy a study was undertaken of A549 cells incubated with complexes **1** and **2** by time-resolved microscopy using a confocal microscope equipped with TRSPC capability. In the present study, fixed (dead) cells were examined so that information relating to e.g. $[O_2]$ is not a useful reflection of live cell conditions, but as a proof of principle study, we were interested to examine the suitability of these agents for time-resolved microscopy, and to obtain lifetime data within cells. As was observed with standard confocal microscopy, both complexes were shown to be taken up well by cells at a variety of concentrations, and accumulated in the cytoplasm, appearing to be associated with a variety of organelles. Both complexes gave good levels of phosphorescence for several weeks after fixing, although **2** showed rapid photobleaching under laser irradiation. As these complexes are highly emissive and dominated over autofluorescence, time gated experiments were not required to separate probe emission from autofluorescence (indeed it was difficult to obtain images of the shorter-lived components which were not dominated by emission from the complexes). However, both time resolved, and time-gated methods worked well in obtaining images which are displayed in Figure 6a, with brightness of a pixel determined by the intensity (photons counted) and the colour of each pixel by lifetime (using the average arrival time of photon after pulse determined from the TRSPC). The long average lifetimes shown in the colours in Figure 6a demonstrate that these are competent probes for time-resolved microscopy (for control images of untreated cells see Figure S21). As can be seen from the scales on the colour bars there was a relatively small variation in average lifetime across the cells, and this was mostly a function of the areas of highest autofluorescence: phosphorescence ratio reducing the average lifetime. Neither the average lifetimes of the decays (200–250 ns for **1** and 350–450 for **2**) nor the longer components (see discussion below) varied significantly across the cells so no mapping of distribution of longer components was attempted. This indicates that the different environments associated with different localisations within the cell had relatively little impact on the phosphorescent lifetime, compared to the overall changes upon entering the cells discussed below. Closer inspection of the lifetime data, however, were intriguing as the average lifetimes observed in the cellular environments were in the order of 300–400 ns for **1** and 400–700 ns **2**, compared to the solution state lifetimes of 376 and 436 ns respectively. In these experiments, in which the average lifetime includes very short lived autofluorescence (typically sub 10 ns), to have average lifetimes so high can imply that much longer components are involved, and to investigate this we examined the cells under laser pulsing conditions which allowed more focus on the phosphorescence. Upon examination of these decay data, using the integrated decays from all pixels for greater statistical power, greater differences from the solution state emerged with the cellular decays fitting best to multi-component decays with long components considerably greater than those observed in solution. In the case of **1** across a number of cells the decays fitted well to a two component model with the major contribution being of around 700 ns, and the minor component (approximately 5 times lower weighted) having a lifetime of around 100 ns. For **2**, again a two component model gave good fits over a number of cells with the major component having a lifetime around 1μs and the minor (approximately 10 times weaker) a lifetime around 100 ns.

It is worth noting that the solution state quantum yields increased in the absence of oxygen by factors of 2–4 (**1** aerated 12.5 %, degassed 26.5 %, **2** aerated 8.5 %, degassed 38.0 %), and, assuming that this reflects solely a decrease in non-radiative decay and no change in excited state emission processes, the

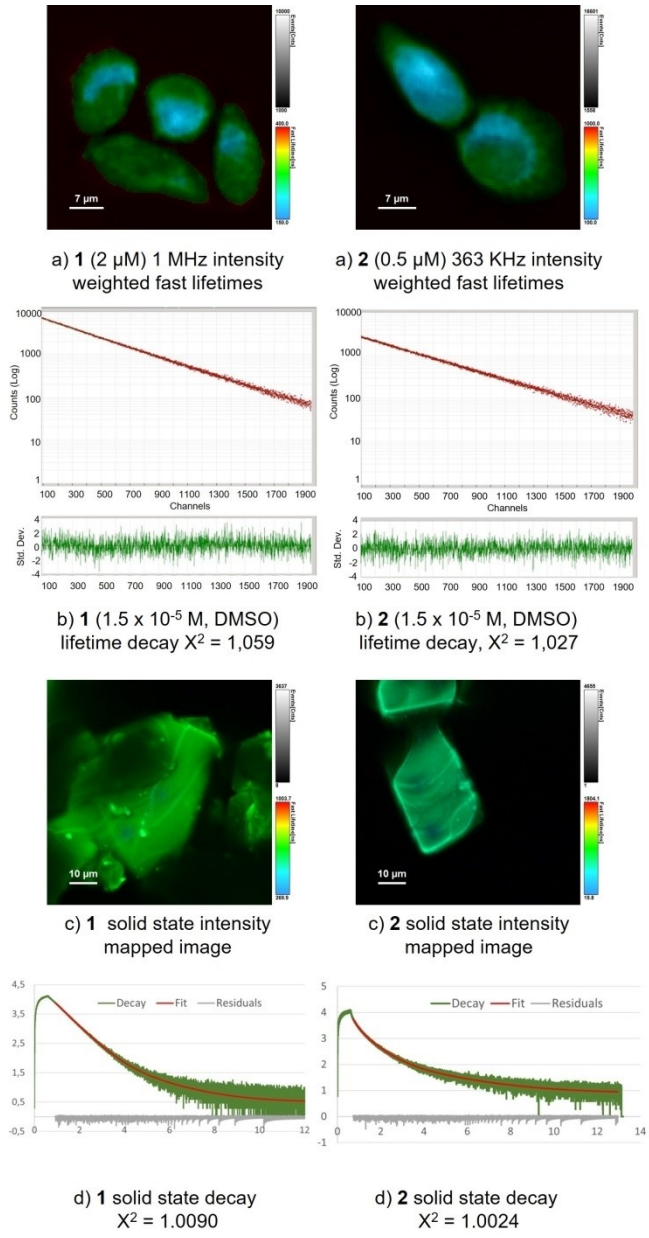

Figure 6. Time-resolved microscopy and decay profiles of (left to right) **1** and **2**. (a) Representative images of fixed A549 cell incubated during 5 hours with **1** and **2** at 2 μM and 0.5 μM, excited at 405 nm detection between 510–700 nm, brightness scale bar = intensity (counts) colour scale bar = average lifetime (ns). (b) Solution state lifetime decay curves of **1** and **2** at 1.5×10^{-5} M in DMSO at 298 K using a 360 nm nanoLED for excitation and detection at 606 and 486 nm respectively. (c) microscope images of solid state complexes, brightness scale bar = intensity (counts) colour scale bar = average lifetime (ns). (c) Solid state lifetime decay curves excited at 405 nm with detection between 510–700 nm.

lifetimes would be predicted to increase proportionally.[48] However, these fixed cells have will not be anaerobic (a typical cellular level in culture is between 1–4 % O_2) and,[49] as absolute anaerobic conditions would be required to explain the longer components, other explanation were explored. As it is likely that in the cellular environment at least a proportion of the complex would be bound to a biomolecule, inside a lipid membrane, or in another environment which is not a true solution we examined the solid-state lifetimes of the complexes. The solid state decay of **1** fitted best to a two component decay comprising of a major contribution from a lifetime of 1663 ns and a minor (approximately 40 times weaker) of 566 ns, see Figure S22. This could be interpreted, given the oxygen-sensitivity of the emission of **1** as resulting from a short surface component (quenched by aerobic oxygen) and a longer interior component, with the surface component more heavily weighted than the molecular ratios would predict due to the poor penetration of excitation through the crystal. However, the longer component is greater than that predicted from the lifetime extension from 376 ns and the change in quantum yield upon degassing, which would predict a maximum of 797 ns. Therefore, it is suggested that reduced molecular vibrations and the lack of interaction with small molecule solvent molecules are likely to also contribute to the extension of lifetime in the solid state. It has previously been noted that triplet-emitting transition metal complexes undergo lifetime and intensity increases when a lipid chain interacts[50] with one of the ligands involved in the photophysical processes, and a similar phenomenon may be responsible for the lifetimes observed here. In the solid state **2** fitted well to a three-component decay with contributions of 2330, 619 and 213 ns, in ratios of relative contribution of 1 : 13 : 14, see Figure S22. Again, the solution state lifetime of 436 ns is predicted by the quantum yield ratios to extend in the absence of oxygen to 1949 ns, but the longest component in the solid state exceeds that suggesting other factors are also important. The existence of two similarly weighted (i.e. unlikely to be surface-related) shorter components also suggest that there are variations in environment (possibly due to crystal packing) also influencing the lifetime in the solid state. Similar values for the extended lifetimes with approximately the same contributions to the decays were observed in several cells (see Figure S23).

Overall, it appears that the decays observed in the cellular environment show the presence of longer-lived components than observed in the solution state, or those predicted for anaerobic conditions, but are not identical to the crystalline state. This may be explained by a combination of binding of complexes to biomolecules, or an accumulation of the lipophilic complexes in relatively immobile cellular structures or components which move some way towards the behaviour seen in the solid state by limiting molecular vibrations, and reducing interactions with small (solvent-like) molecules. Is should be noted that binding of iridium complexes to certain biomolecules *in vitro*[51] has been reported to lead to lifetime extensions, although to the best of our knowledge this is as yet unexplored in cell microscopy studies of related complexes.

Conclusion

In summary, two cyclometallated Ir(III) complexes of the general formula $[Ir(ppy)_2(\mathbf{L1}/\mathbf{L2})]Cl$, where **L1** is 1-((quinolinyl)-2-metyl)-2-(2-pyridyl)benzimidazole and **L2** is 1-((quinolinyl)-2-metyl)-2-(4-thiazolyl)benzimidazole have been synthesised following

well-stablished synthetic methods. Varying the substituent on the benzimidazole ligand, from 2-pyridyl in **L1** to a 4-thiazolyl in **L2** induces large differences in the photophysical properties of complexes **1** and **2**, while their antiproliferative activity and cellular biodistribution in A549 cells remain comparable. Thus, compound **1** has orange emission due to a mixture of ^{3}MLCT and ^{3}LLCT process, whereas compound **2** emits a green color due to mainly a ^{3}LC transition. The quantum yield of complex **1** increased two-fold upon deoxygenation of the solvent reaching a value of 0.26. For complex **2** the value increased more than four times reaching a quantum yield efficiency of 0.36 and revealing the higher speed of deactivation via a non-radiative process. Regarding their antiproliferative potential in A549 cells, both showed similar behaviour, with IC_{50} values in the low micromolar range (4.59 ± 0.23 μM (**1**) and 3.50 ± 0.17 μM (**2**)). In contrast, neither **L1** nor **L2** were cytotoxic at the concentrations studied. Antiproliferative activity of both complexes increased up to ca. 15 times upon irradiation at 470 nm suggesting their potential viability for photodynamic therapy purposes. In addition, ROS generation assay demonstrates the greater production of ROS of complex **2** under irradiation conditions, which goes in line with the higher antiproliferative potential seen. Direct detection of singlet oxygen emission by fluorescence spectroscopy, revealed that such species was being produced upon irradiation. Preliminary cellular biodistribution was addressed by fluorescence microscopy in live cells, suggesting lysosomes as the main accumulation domain and revealing faster photobleaching of compound **2** in comparison with **1**. Similarly, time-resolved and time-gated florescence microscopy was used in fixed cells, utilizing the long luminescent lifetimes and demonstrating the viability of **1** and **2** as probes for time-resolved imaging. These studies corroborated the cellular permeation of the complexes and their preferential accumulation in some domains within the cytoplasm, along with the rapid photobleaching of complex **2**. On top of that, close examination of the lifetime data of complexes collected by time-resolve fluorescence microscopy in fixed cells, and their comparison with the lifetime values in solution, solid state, and in absence of oxygen, indicated that the cellular lifetimes are significantly longer than the solution ones, even when lower oxygen concentrations are considered. These observations suggest the possibility of either interaction between the complexes and biomolecules and/or their confinement within relatively immobile cellular structures or compartments, proposing that time-resolved techniques may be useful not only for elucidating cellular biodistribution of the probes but also in revealing their molecular-level interactions within the cells. In conclusion, the Ir(III) benzimidazole-quinoline complexes described in here presented tunable photophysical properties ideal to be used either fluorescence and time resolved microscopy. In addition, their great potential in chemotherapy and photodynamic therapy makes them very promising lead candidates for the development of future theranostic agents.

Experimental Section

Materials and instrumentation: ^{1}H and ^{13}C-{^{1}H} NMR, including 2D experiments, were recorded at room temperature (rt) on a BRUKER AVANCE 400 spectrometer (^{1}H-400 MHz, ^{13}C-100.6 MHz) with chemical shifts (δ, ppm) reported relative to the solvent peaks of the deuterated solvent[52] Mass spectra were recorded on a BRUKER ESQUIRE 3000 PLUS, with the electrospray (ESI) technique. Steady-state photoluminescence spectra were recorded with a Jobin-Yvon-Horiba fluorolog FL-3-11 spectrometer using band pathways of 3 nm for both excitation and emission. Nanosecond lifetimes in solution were recorded with a Datastation HUB-B with a nanoLED controller and software DAS6. The nanoLEDs employed for lifetime measurements was of 390 nm, emission was set to 606 and 486 nm for complexes **1** and **2** respectively. The lifetime data were fitted using the Jobin-Yvon software package. UV–Vis spectra were recorded with 1 cm quartz cells on an Evolution 600 spectrophotometer. Quantum yields were measured using an absolute method provided by Hamamatsu Photonics Quantaurus-QY C11347-11. Specifically, each sample was measured using the excitation scanning mode (exciting from 350 to 500 mn for complex **1** and from 320 to 450 nm for **2**) in aerated and non-aerated DMSO solution of both complexes at 1.10^{-5} M, at room temperature (rt) after recording a reference sample (neat aerated and non-aerated DMSO at rt respectively). The quantum yield value given is the one obtained at intensity excitation of 440 nm for each complex. The experiment was repeated three times to ensure reproducibility.

Cell culture: A549 (human lung carcinoma) cell line was routinely cultured in high glucose DMEM medium supplemented with 5% fetal bovine serum (FBS), L-glutamine and penicillin/streptomycin at 37 °C in a humidified atmosphere of 95% air/5% CO_2.

Cell proliferation assays: The MTT-reduction assay was used to analyse cell metabolic activity as an indicator for cell sensitivity to the complexes in A549 cell line. 10^5 cells/mL were seeded in complete medium in flat-bottom, 96-well plates (100 μL/well) and allowed to attach for 24 h prior to addition of compounds. Working solutions serially diluted of the complex and ligand ranging from 0.2 to 50 μM were prepared using cellular media DMEM and starting from DMSO stock of the compounds at 0.1 M. Thereafter, compounds were added to the cells in quadruplicate for each concentration, containing the more concentrated sample 2% of DMSO. After 4 h of incubation with the complexes, duplicates of each concentration were irradiated with a monochromatic led of 470 nm, 15.2 $J \cdot cm^{-2}$, for 10 min. Prior to this, culture medium was replaced with fresh medium in order to avoid interference with non-internalised complexes. Cells were cultured for further 20 h, then 10 μL of MTT (5 mg ml^{-1} in PBS) was added to each well and plates were incubated for 2 h at 37 °C. Finally, culture medium was removed and DMSO (100 μL/well) was added to dissolve the formazan crystals. The optical density was measured at 550 nm using a 96-well multiscanner autoreader (ELISA) and IC_{50} values were calculated. Each compound was analysed at least in three independent experiments.

ROS generation. 1×10^5 A549 cells/well were seeded in complete medium in flat-bottom, 12-well plates (1 mL/well) and allowed to attach for 24 h prior to addition of the compound. Complex **2** was dissolved in DMSO and added to cells up to concentration of 0.3, 0.5 and 0.75 μM in triplicate for dark and under irradiation conditions. Cells were incubated with the complex for 5 h and subsequently half of the experimental points were irradiated at 470 nm after replacing culture medium. Upon 19 h, cells were trypsinized, resuspended in 100 μL of a mixture of PBS and 2 μM of the dihydroethidium (DHE) probe, incubated at 37 °C in the dark for 15 minutes and diluted to 200 μL with PBS. Lastly, a total of 10,000 events were acquired on a FACSCalibur™ flow cytometer

and data were analyzed using the aforementioned software platforms.

Singlet oxygen detection. Singlet oxygen emission spectra were measured on a PicoQuant, FT300 fluorescence spectrometer equipped with a Hamamatsu H10330 A-45 thermoelectric cooled NIR-PMT unit with a spectral range of 950 nm to 1400 nm. Complex **2** (1.13 μM in CH_3CN) were excited with a 405 nm picosecond pulsed diode laser (P-C-405, PicoQuant) with 80 MHz repetition rate. Signals were digitised with a Time Harp 260 PCI card (PicoQuant). Spectra were recorded in the custom measurement mode of EasyTau software with the settings: laser intensity: 10.0; excitation attenuator: open; emission attenuator: 100%; Bandwidth 20.6 nm; delta 0.5 nm; integration time: 0.5 s. Spectra for the titration were run under the same conditions but with delta: 1 nm; integration time 0.1 s.

Fluorescence confocal microscopy assays: 10^4 A549 cells/well were seeded in complete medium in μ-slide 8 well (ibiTreat) (300 μL/well) and left 24 h to be attached to the bottom. Then, 200 μL of culture medium were removed and 100 μL of a solution of the corresponding complexes were added to a final concentration of 2 μM. The complexes were incubated with the cells for 2 h. Thereafter, MitoTracker Deep Red (MTDR) and LysoTracker Red (LTR) were added to final concentrations of 250 nM and 100 nM, respectively. They were incubated with the cells for 45 min at rt. Images were collected in a sequential mode in a ZEISS LSM 880 confocal microscope with a 63 oil immersion lens, a line average of 4, and a format of 1024×1024 pixels using excitation wavelength of either 405 nm (detection window between 482 and 677 nm), 561 nm (detection window between 570 and 615 nm) and 633 nm-(detection window between 638 and 758 nm). The confocal pinhole was 1 Airy unit. Images were analysed with ZEISS ZEN lite (blue edition) software.

Time resolved microscopy: European Collection of Cell Cultures, were maintained in HEPES modified minimum essential medium (DMEM) supplemented with 10% fetal bovine serum, penicillin, and streptomycin. A549 cells were detached from the plastic flask using trypsin-EDTA solution and suspended in an excess volume of growth medium. The homogeneous cell suspension was then distributed into 24-well flat-bottomed microplates over a cover slip placed inside each well and they were allowed to attach for 24 h prior to addition of compounds. Complexes were added (10 μL) to the cells up to final concentrations of 0.5 and 2 μM for compounds **1** and **2**. After incubation for 5 h at 37 °C, the growth medium was removed and PBS was added for a washing step (3×0.5 mL). Thereafter, 0.5 ml of paraformaldehyde (4%) was added and allowed to stand for 15 min at room temperature. Eventually the paraformaldehyde was removed and further washings with PBS were performed (3×0.5 mL). The cover slips were collected from the 24 well plate, immersed for 1 or 2 seconds in distilled water and let them to drip the water. Then, they were placed over a microscope slide where a drop of fluoromont was previously placed. Time resolved microscopy images and data were collected on a MicroTime 200 (PicoQuant) time resolved confocal fluorescence microscopy system consisting of an Olympus IX73 confocal microscope fitted with a ×100 oil objective excited with a picosecond pulsed 405 nm laser at the repetition rates referenced in the individual images. The emitted fluorescence was spectrally cleaned with a dichroic mirror and a transmission band edge filter (510 nm). A pinhole of 50 microns was employed to reject light that was out of focus. The fluorescence was detected using single photon counting with an avalanche diode (SPAD-100, PicoQuant) and digitised with a Time Harp 260 PCI card (PicoQuant). The images were generated using the SymphoTime 64 software package and all decay profiles were analysed using multiexponential models via an iterative reconvolution process using SymPhoTime software (PicoQuant). Fit quality was assessed from the χ^2 parameter and weighted residuals.

Photobleaching assays: Emission of complexes **1** and **2** in DMSO at 10^{-4} M, combined with 20 μL of LysoTracker Green (LTG) at 10^{-4} M (DMSO) were measured using a Jobin-Yvon-Horiba fluorolog FL-3-11 spectrometer at room temperature. The emission spectra were collected before and after irradiation with a UV lamp of 365 nm using cycles of 2 minutes irradiation.

Starting Materials: The starting complex $[Ir(ppy)_2(\mu\text{-}Cl)]_2$, was prepared according to published procedures.[36] All other reagents were commercially available. Solvents were used without purification or drying, and all manipulations were performed in aerated atmosphere.

Synthetic procedure of ligands L1 and L2:

1-((quinolinyl)-2-metyl)-2-(2-pyridyl)benzimidazole (L1): 2-(2-pyridyl)- benzimidazole (300 mg; 1.54 mmol) was dissolved in 4 ml of DMF. An excess of K_2CO_3 (637 mg; 4.62 mmol) was added to the initial solution, and the reaction mixture was stirred at r.t. for 30 min. Then, a solution of 2-chlorometylquinoline (329 mg; 1.54 mmol) in 1 ml of DMF was added, and the mixture was stirred at r.t. for 48 hours. After this time, the yellow solid precipitated was filtered and washed with water (3×4 ml) to remove the unreacted carbonate and potassium salts. Thereafter, the solid collected was dissolved in DCM (17 ml) and further dried with $MgSO_4$, which was removed from the solution by gravity filtration. The volume of the resultant yellow solution was reduced, and the addition of diethyl ether afforded the desired compound as a white solid, which was isolated by filtration. (58%; 302 mg). ^{1}H NMR (400 MHz, $CDCl_3$) δ 8.56 (ddd, J = 4.8, 1.8, 1.0 Hz, 1H, CH (b)), 8.52 (dt, J = 8.0, 1.1 Hz, 1H, CH (e)), 8.12 (dq, J = 7.8, 1.1 Hz, 1H, CH (s)), 7.97 (dd, J = 8.6, 0.8 Hz, 1H, CH (q)), 7.91–7.82 (m, 2H, CH (j, d)), 7.74 (td, J = 7.6, 1.3 Hz, 2H, CH (t, v)), 7.52 (td, J = 7.3, 1.2 Hz, 1H, CH (u)), 7.41 (dt, J = 8.1, 1.0 Hz, 1H, CH (m)), 7.34–7.28 (m, 2H, CH (k, c)), 7.23 (ddd, J = 8.2, 7.2, 1.2 Hz, 1H, CH (l)), 7.09 (d, J = 8.5 Hz, 1H, CH (p)), 6.48 (s, 2H, (CH_2)) ppm. ^{13}C NMR (101 MHz, $CDCl_3$) δ 158.0 (C (f)), 150.4 (C (i)), 150.0 (C (o)), 148.8 (C (b)), 147.8 (C (n)), 142.8 (C (w)), 137.2 (C (q)), 137.1 (C (d)), 137.0 (C (g)), 129.9 (C (v)), 129.1 (C (s)), 127.8 (C (t)), 127.5 (C (r)), 126.6 (C (u)), 124.8 (C (e)), 124.1 (C (l)), 124.0 (C (k)), 123.2 (C (c)), 120.2 (C (j)), 119.0 (C (p)), 111.1 (C (m)), 52.1 (C (CH_2)) ppm. HRMS (ESI): m/z (calcd.) = 337.1353, m/z (found) = 337.1452.

1-((quinolinyl)-2-metyl)-2-(4-thiazolyl)benzimidazole (L2): 2-(4-thiazolyl)benzimidazole (200 mg, 1 mmol) was dissolved in 7 ml of CH_3CN and an excess of KOH was added. The resultant white suspension was stirred for 10 min, and 2-chloromethylquinoline (222.0 mg; 1 mmol) was added. The mixture was stirred at r.t. for 48 h. Thereafter the solvent was removed affording a white solid, which was washed with water several times to remove the unreacted KOH and potassium salts formed during the reaction. Then, the solid was partially dissolved in DCM (5 ml×4) and the liquid layer separated by centrifugation. Finally evaporation of the DCM rendered the desired product as a white solid (75%; 256 mg). ^{1}H NMR (400 MHz, $CDCl_3$) δ 8.85 (d, J = 2.2 Hz, 1H, (CH (b)), 8.41 (d, J = 2.2 Hz, 1H (CH, (d)), 8.12 (dd, J = 8.2, 1.0 Hz 1H, (CH (s)), 7.97 (dd, J = 8.5, 0.8 Hz, 1H, (CH (q)), 7.84 (dt, J = 8.1, 1.0 Hz, 1H, (CH (i)), 7.77–7.71 (m, 2H, (CH (t, v)), 7.52 (ddd, J = 8.2, 7.0, 1.2 Hz, 1H, (CH (u)), 7.39 (dt, J = 8.0, 1.0 Hz, 1H, (CH (l)), 7.30 (ddd, J = 8.2, 7.2, 1.2 Hz, 1H, CH (j)), 7.21 (ddd, J = 8.2, 7.2, 1.2 Hz, 1H (CH (k)), 7.04 (d, J = 8.5 Hz, 1H, (CH (p)), 6.37 (s, 2H, (CH_2) ppm. ^{13}C NMR (101 MHz, $CDCl_3$) δ 157.6 (C (o)), 153.3 (C (b)), 147.9 (C (w)), 147.8 (C (h)), 147.1 (C (e)), 143.2 (C (q)), 137.4 (C (m)), 136.2 (C (v)), 130.0 (C (s)), 129.2 (C (f)), 127.8 (C (t)), 127.5 (C (u)), 126.6 (C (r)), 123.6 (C (k)), 123.2 (C (j)),

121.6 (C (d)), 119.9 (C (i)), 118.8 (C (p)), 111.0 (C (l)), 51.6 (CH_2) ppm. HRMS (ESI): m/z (calcd.) = 34.1017, m/z (found) = 343.1024.

Synthetic procedure of complexes 1 and 2:

Complex 1: $[Ir(ppy)_2(\mu\text{-}Cl)]_2$ (55 mg; 0.050 mmol) and **L1** (34.38 mg; 0.10 mmol) was stirred and heated to reflux for 24 h in a mixture DCM:MeOH (1:3). The resultant yellow suspension was filtered and the filtrate was dried under vacuum. The purification process was carried out by column chromatography in silica gel using a mixture of DCM:MeOH (9:1). The desired product was obtained as a red solid. (23%; 20 mg). ^{1}H NMR (400 MHz,$CDCl_3$) δ 9.04 (s_{broad}, 1H (CH, (e)), 8.31 (s_{broad}, 1H (CH, (s)), 8.23 (d, J = 7.3 Hz, 1H (CH, (q)), 8.04 (m, 1H (CH, (d), 7.85–7.85 (m, 4H (CH, (3, 3', b, 6)), 7.75–7.60 (m, 5H (CH, (p, 4, 4', 9, 9'), 7.57 (d, J = 8.4 Hz, 1H (CH, (m)), 7.51 (d, J = 5.3, 1H (CH, (6')), 7.48–7.37 (m, 2H, (CH, (v, u)), 7.33 (t, J = 7.7 Hz, 1H (CH, (t)), 7.26 (t, 1H (CH, (l)), 7.21 (t, 1H (CH, (c)), 7.13–7.06 (m, 2H, (CH, (10)), CH_2), 7.05–6.87 (m, 6H (CH, (k, 10', 5, 5', 11, 11')), 6.70 (d, J = 17.2 Hz, 1H, CH_2), 6.43 (dd, J = 7.6, 1.2 Hz, 1H (CH, (12)), 6.37 (d, J = 8.3 Hz 1H (CH, (j)), 6.26 (dd, J = 7.6, 1.2 Hz, 1H (CH, (12')) ppm. ^{13}C NMR (101 MHz, $CDCl_3$) δ 168.3 (C (2)), 168.2 (C (2')), 154.5 (C (f/o)), 153.6 (C (f/o)), 152.2 (C (g)), 150.9 (C (b)), 149.7 (C (6)), 149.0 (C (6')), 147.8 (C (8/8'/w)), 147.7 (C (8/8'/w)), 147.5 (C (8/8'/w)), 144.3 (C (7)), 143.9 (C (7')), 140.4 (C (d)), 139.5 (C (i)), 137.8 (C (4/4'/q/n)), 137.7 (C (4/4'/q/n)), 137.5 (C (4/4'/q/n)), 137.4 (C (4/4'/q/n)), 132.5 (C (12)), 131.8 (C (12')), 131.0 (C (11)), 130.2 (C (11')), 129.1 (C (v/p)), 128.9 (C (v/p)), 128.1 (C (l)), 127.9 (C (r)), 127.5 (C (e)), 127.4 (C (c)), 126.5 (C (u)), 126.1 (C (t)), 125.1 (C (k)), 124.9 (C (9)), 124.7 (C (9')), 123.3 (C (5)), 123.2 (C (5')), 122.6 (C (10)), 122.4 (C (10')), 121.4 (C (s)), 119.5 (C (3)), 119.4 (C (3')), 118.3 (C (j)), 111.9 (C (m)), 50.9 (C (CH_2)) ppm. HRMS (ESI): m/z (calcd.) = 837.2294, m/z (found) = 837.2301.

Complex 2: $[Ir(ppy)_2(\mu\text{-}Cl)]_2$ (70 mg, 0.065 mmol) and **L2** (46.46 mg; 0.13 mmol) was stirred and heated to reflux for 24 h in 5 ml of dichloromethane. The volume of the resultant solution was reduced until minimum volume, and hexane was added affording the precipitation of a red solid. The solid was isolated by filtration and washed with hexane (3 × 4 ml). The purification process was carried out by column chromatography in silica gel using a mixture of DCM:MeOH (9:1). The desired product was obtained as a red solid (60 mg, 61%). ^{1}H NMR (400 MHz, $CDCl_3$) δ 9.75 (d, J = 1.9 Hz, 1H (CH, (d)), 8.28–8.14 (m, 2H (CH, (q, s)), 8.07 (d, J = 1.7 Hz, 1H (CH, (b)), 7.96–7.83 (m, 3H (CH, (6, 3, 3')), 7.79–7.68 (m, 4H (CH, (4, 4', 9, t)), 7.65 (dd, J = 7.8, 1.3 Hz, 1H (CH, (9')), 7.57–7.39 (m, 4H (CH, (6', l, v, u)), 7.35–7.26 (m, 2H (CH, (p, k)), 7.09 (td, J = 7.5, 1.2 Hz, 1H (CH, (10)), 7.05–6.82 (m, 7H (CH, (5, 5', 10', 11, 11', j), CH_2), 6.61–6.44 (m, 2H (CH, (12), CH2), 6.40–6.28 (m, 2H, (CH, (12', i)) ppm. ^{13}C NMR (101 MHz, $CDCl_3$) δ 168.3 (C (2)), 168.2 (C (2')), 155.1 (C (b/o)), 154.2 (C (b/o)), 149.8 (C (6)), 149.5 (C (7)), 148.9 (C (e)), 148.7 (C (6')), 147.5 (C (f)), 147.4 (C (7')), 144.4 (C (8)), 144.3 (C (8')), 144.2 (C (w)), 139.5 (C (h)), 137.9 (C (4)), 137.7 (C (4')), 137.4 (C (q)), 137.0 (C (m)), 132.5 (C (12)), 132.2 (C (12')), 130.6 (C (11)), 130.2 (C (11')), 129.1 (C (p)), 129.1 (C (v)), 128.1 (C (t)), 127.9 (C (u)), 127.5 (C (d)), 126.6 (C (r)), 125.4 (C (k)), 124.8 (C (j)), 124.7 (C (9)), 124.6 (C (9')), 123.2 (C (5)), 123.1 (C (5')), 122.6 (C (10)), 122.4 (C (10')), 121.2 (C (s)), 119.4 (C (3)), 119.3 (C (3')), 118.0 (C (i)), 111.6 (C (l)), 50.1 (C (CH_2)) ppm. HRMS (ESI): m/z (calcd.) = 843.1882, m/z (found) = 843.1862.

Acknowledgements

Authors thank the Agencia Estatal de Investigación, projects PID2019-104379RB-C21/AEI/10.13039/501100011033, RTI2018-097836-J-I00/MCIN/AEI/10.13039/501100011033/FEDER, RYC2018-025872-I (funded by MCIN/AEI/10.13039/501100011033 and by "ESF Investing in your future"), RED2018-102471-T/MCIN/AEI/10.13039/501100011033, and Gobierno de Aragón-Fondo Social Europeo (E07_20R) for financial support. M. R. thanks the Gobierno de Aragón for a predoctoral fellowship.

Conflict of Interest

The authors declare no conflict of interest.

Data Availability Statement

The data that support the findings of this study are available in the supplementary material of this article.

Keywords: FLIM · bioimaging · iridium · anticancer · cytotoxicity

[1] R. Paprocka, M. Wiese-Szadkowska, S. Janciauskiene, T. Kosmalski, M. Kulik, A. Helmin-Basa, *Coord. Chem. Rev.* **2022**, *452*, 214307–214328.
[2] Z. Fan, Y. Rong, T. Sadhukhan, S. Liang, W. Li, Z. Yuan, Zilin Zhu, S. Guo, S. Ji, J. Wang, R. Kushwaha, S. Banerjee, K. Raghavachari, H. Huang, *Angew. Chem. Int. Ed.* **2022**, e202202098.
[3] M. Redrado, A. Benedi, I. Marzo, A. L. García-Otín, V. Fernández-Moreira, M. C. Gimeno, *Chem. Eur. J.* **2021**, *27*, 9885–9897.
[4] M. Redrado, V. Fernández-Moreira, M. C. Gimeno, *ChemMedChem* **2021**, *16*, 932–941.
[5] L. R. Kelland, *Drugs* **2000**, *59*, 1–8.
[6] S. Dasari, P. B. Tchounwou, *Eur. J. Pharmacol.* **2014**, *740*, 364–378.
[7] X. Liao, J. Shen, W. Wu, S. Kuang, M. Lin, J. Karges, Zilong Tang, H. Chao, *Inorg. Chem. Front.* **2021**, *8*, 5045–5053.
[8] C. Caporale, M. Massi, *Coord. Chem. Rev.* **2018**, *363*, 71–91.
[9] H. Huang, S. Banerjee, K. Qiu, P. Zhang, O. Blacque, T. Malcomson, M. J. Paterson, G. J. Clarkson, M. Staniforth, V. G. Stavros, G. Gasser, H. Chao, P. J. Sadler, *Nat. Chem.* **2019**, *11*, 1041–1048.
[10] Q. Zhao, M. Yu, L. Shi, S. Liu, C. Li, M. Shi, Z. Zhou, C. Huang, F. Li, *Organometallics* **2010**, *29*, 1085–1091.
[11] R. Guan, L. Xie, L. Ji, H. Chao, *Eur. J. Inorg. Chem.* **2020**, *42*, 3978–3989.
[12] N. Johnsson, K. Johnsson, *ACS Chem. Biol.* **2007**, *2*, 1, 31–38.
[13] Z. Liu, Z. Bian, C. Huang, *Top. Organomet. Chem.* Springer-Verlag Berlin Heidelberg **2010**, *28*, 113–142.
[14] A. Zamora, G. Vigueras, V. Rodríguez, M. D. Santana, J. Ruiz, *Coord. Chem. Rev.* **2018**, *360*, 34–76.
[15] J. Karges, H. Chao, G. Gasser, *JBIC J. Biol. Inorg. Chem.* **2020**, *25*,1035–1050.
[16] J. S. Nam, M.-G. Kang, J. Kang, S.-Y. Park, S. J. C. Lee, H.-T. Kim, J. K. Seo, O.-H Kwon, M. H. Lim, H.-W. Rhee, T.-H. Kwon, *J. Am. Chem. Soc.* **2016**, *138*, 34, 10968–10977.
[17] L. Murphy, A. Congreve, L.-O. Pålssona, J. A. Gareth Williams, *Chem. Commun.* **2010**, *46*, 8743–8745.
[18] A. Mills, *Platinum Metals Rev.* **1997**, *41*(3), 115–127.
[19] W. Zhong, P. Urayama, M.-A. Mycek, *J. Phys. D* **2003**, *36*, 1689–1695.
[20] S. M. Sternisha, P. Mukherjee, A. Alex, E. J. Chaney, R. Barkalifa, B. Wan, J. H. Lee, J. Rico-Jimenez, M. Žurauskas, D. R. Jr Spillman, S. A. Sripada, M. Marjanovic, Z. Arp, S. S. Galosy, D. S. Bhanushali, S. R. Hood, S. Bose, S. A. Boppart, *Biotechnol. J.* **2021**, *16*(7), e2000629.
[21] G. S. Miller, R. M. Parente, S. Santra, A. J. Gesquiere, *Planta* **2021**, *253*, 62.
[22] J. R. Lakowicz, in *Principles of Fluorescence Spectroscopy*, Springer, Boston, **2006**.
[23] E. Baggaley, S. W. Botchway, J. W. Haycock, H. Morris, I. V. Sazanovich, J. A. G. Williams, J. A. Weinstein, *Chem. Sci.* **2014**, *5*, 879–886.
[24] M. Boiani, M. González, *Mini-Rev. Med. Chem.* **2005**, *5*(4), 409–424.
[25] S. Tahlan, S. Kumar, S. Kakkar, B. Narasimhan, *BMC Chemistry* **2019**, *13*, 66–82.

[26] L. K. McKenzie, I. V. Sazanovich, E. Baggaley, M. Bonneau, V. Guerchais, J. A. G. Williams, J. A. Weinstein, H. E. Bryant, *Chem. Eur. J.* **2017**, *23*, 234–238.
[27] J. Yellol, S. A. Pérez, G. Yellol, J. Zajac, A. Donaire, G. Vigueras, V. Novohradsky, C. Janiak, V. Brabec, J. Ruiz, *Chem. Commun.* **2016**, *52*, 14165–14168.
[28] L. He, Y. Li, C.-P. Tan, R.-R. Ye, M.-H. Chen, J.-J. Cao, L.-N. Ji, Z.-W. Mao, *Chem. Sci.* **2015**, *6*, 5409–5420.
[29] R. Liu, D. Ma, C. Zhang, L. Duan, *Dalton Trans.* **2019**, *48*, 9669–9675.
[30] I. Echevarría, M. Vaquero, B. R. Manzano, F. A. Jalón, R. Quesada, G. Espino, *Inorg. Chem.* **2022**, *61*, 6193—6298.
[31] V. Novohradsky, A. Zamora, A. Gandioso, V. Brabec, J. Ruiz, V. Marchán, *Chem. Commun.* **2017**, *53*, 5523–5526.
[32] E. Zafon, I. Echevarría, S. Barrabés, B. R. Manzano, F. A. Jalón, A. M. Rodríguez, A. Massaguer, G. Espino, *Dalton Trans.* **2022**, *51*, 111–128.
[33] F.-X. Wang, M.-H. Chen, Y.-N. Lin, H. Zhang, C.-P. Tan, L.-N. Ji, Z.-W. Mao, *ACS Appl. Mater. Interfaces* **2017**, *9*, 42471–42481.
[34] N. M. Shavaleev, Z. R. Bell, T. L. Easun, R. Rutkaite, L. Swanson, M. D. Ward, *Dalton Trans.* **2004**, 3678–3688.
[35] M. Vaquero, N. Busto, N. Fernández-Pampín, G. Espino, B. García, *Inorg. Chem.* **2020**, *59*, 4961–4971.
[36] S. Sprouse, K. A. King, P. J. Spellane, R. J. Watts, *J. Am. Chem. Soc.* **1984**, *106*, 22, 6647–6653.
[37] D. Ma, C. Zhang, R. Liu, Y. Qiu, L. Duan, *Chem. Eur. J.* **2018**, *24*, 5574–5583.
[38] C. D. Ertl, J. Cerdá, J. M. Junquera-Hernández, A. Pertegás, H. J. Bolink, E. C. Constable, M. Neuburger, E. Ortí, C. E. Housecroft, *RSC Adv.* **2015**, *5*, 42815–42827.
[39] M. Martínez-Alonso, J. Cerdá, C. Momblona, A. Pertegás, J. M. Junquera-Hernández, A. Heras, A. M. Rodríguez, G. Espino, H. Bolink, E. Ortí, *Inorg. Chem.* **2017**, *56*, 17, 10298–10310.
[40] M. S. Lowry, W. R. Hudson, R. A. Pascal Jr., S. Bernhard, *J. Am. Chem. Soc.* **2004**, *126*, 14129–14135.
[41] M. Redrado, A. Benedi, I. Marzo, M. C. Gimeno, V. Fernández-Moreira, *Pharmaceutica* **2021**, *13*, 1382.
[42] C. Perez-Arnaiz, M. I. Acuña, N. Busto, I. Echevarría, M. Martínez-Alonso, G. Espino, B. García, F. Domínguez, *Eur. J. Med. Chem.* **2018**, *157*, 279–293.
[43] C. Caporale, M. Massi, *Coord. Chem. Rev.* **2018**, *363*, 71–91.
[44] G. Vigueras, L. Markova, V. Novohradsky, A. Marco, N. Cutillas, H. Kostrhunova, J. Kasparkova, J. Ruiz, V. Brabec, *Inorg. Chem. Front.* **2021**, *8*, 4696–4711.
[45] L. Wang, S. Monro, P. Cui, H. Yin, B. Liu, C. G. Cameron, W. Xu, M. Hetu, A. Fuller, S. Kilina, S. A. McFarland, W. Sun, *ACS Appl Mater. Interfaces* **2019**, *11*, 3629–3644.
[46] A. A. Gorman, M. A. J. Rodgers, *J. Photochem. Photobiol. B* **1992**, *14*, 159–176.
[47] K. W. Dunn, M. M. Kamocka, J. H. McDonald, *Am. J. Physiol. Cell Physiol.* **2011**, *300*, C723–C742. Note: Online free software ZEN Lite was used for the calculation of Person coefficient.
[48] D. M. Jameson, in *Introduction to Fluorescence*, CRC Press, New York, **2014**.
[49] J. A. Stuart, J. Fonseca, F. Moradi, C. Cunningham, B. Seliman, C. R. Worsfold, S. Dolan, J. Abando, L. A. Maddalena, *Oxid Med Cell Longev.* **2018**, *2018*, 8238459.
[50] M. P. Coogan, V. Fernández-Moreira, J. B. Hess, S. J. A. Pope, C. Williams, *New J. Chem.* **2009**, *33*, 1094–1099.
[51] K. K.-W. Lo, K. Y. Zhang, S.-K. Leung, M.-C. Tang, *Angew. Chem. Int. Ed.* **2008**, *47*, 2213–2216; *Angew. Chem.* **2008**, *120*, 2245–2248.
[52] G. R. Fulmer, A. J. M. Miller, N. H. Sherden, H. E. Gottlieb, A. Nudelman, B. M. Stoltz, J. E. Bercaw, K. I. Goldberg, *Organometallics* **2010**, *29*, 2176–2179.

Manuscript received: May 3, 2022
Revised manuscript received: June 28, 2022
Accepted manuscript online: June 29, 2022
Version of record online: July 13, 2022